Analysis of instrument self-noise and microseismic event detection using power spectral density estimates

Y. Vaezi and M. van der Baan

Department of Physics, University of Alberta, Edmonton, AB, Canada T6G 2E1. E-mail: yvaezi@ualberta.ca

SUMMARY

Reliability of microseismic interpretations is very much dependent on how robustly microseismic events are detected and picked. Various event detection algorithms are available but detection of weak events is a common challenge. Apart from the event magnitude, hypocentral distance, and background noise level, the instrument self-noise can also act as a major constraint for the detection of weak microseismic events in particular for borehole deployments in quiet environments such as below 1.5–2 km depths. Instrument self-noise levels that are comparable or above background noise levels may not only complicate detection of weak events at larger distances but also challenge methods such as seismic interferometry which aim at analysis of coherent features in ambient noise wavefields to reveal subsurface structure. In this paper, we use power spectral densities to estimate the instrument self-noise for a borehole data set acquired during a hydraulic fracturing stimulation using modified 4.5-Hz geophones. We analyse temporal changes in recorded noise levels and their time-frequency variations for borehole and surface sensors and conclude that instrument noise is a limiting factor in the borehole setting, impeding successful event detection. Next we suggest that the variations of the spectral powers in a time-frequency representation can be used as a new criterion for event detection. Compared to the common short-time average/long-time average method, our suggested approach requires a similar number of parameters but with more flexibility in their choice. It detects small events with anomalous spectral powers with respect to an estimated background noise spectrum with the added advantage that no bandpass filtering is required prior to event detection.

Key words: Fourier analysis; Downhole methods; Interferometry.

1 INTRODUCTION

Microseismic monitoring involves the acquisition of continuous seismic data for the purpose of locating and characterizing microseismicity induced by hydraulic fracturing due to fluid injection, monitoring resulting reservoir changes, and understanding the associated geomechanical processes in the subsurface. Its wide applications in hydrofracture monitoring, geothermal studies, reservoir surveillance, and monitoring of CO_2 sequestration have turned microseismic monitoring into an invaluable tool (Phillips *et al.* 2002; Maxwell *et al.* 2004; Warpinski 2009; van der Baan *et al.*, 2013). Microseismicity should not be confused with 'microseism' which is the term commonly used to describe the strong and continuous peak in the spectra of the Earth noise field dominantly observed in the period range of 4–20 s and is related to ocean waves' interactions (Lee 1935; Ewing *et al.* 1957). In this paper, we strictly adhere to the term 'microseismic event' to describe microearhquakes which are typically known as earthquakes with magnitudes below zero (Maxwell *et al.* 2010). Microseismic monitoring differs in many

respects from seismic reflection surveys that are traditionally used for oil and gas exploration and development, including the type of sources, receivers and methods of analysis. Microseismic data are typically broadband (10–1000 Hz) and recorded at high sampling rates with three-component surface and/or borehole receivers. A crucial step in the processing of microseismic data is event detection and time picking that should be done accurately. Any errors in the onset-time picking may be amplified when locating or identifying the events, and performing source mechanism analysis.

Microseismic data are mostly acquired continuously and comprise therefore large volumes. Manual detection is subjective and time consuming. Therefore, an automatic event detection algorithm is required to make this process economic in terms of computation time and effort. There are a great number of trigger algorithms available for onset-time picking that are generally characterized into time domain, frequency domain, particle motion processing, or pattern matching (Withers *et al.* 1998). All of these algorithms are either based on the amplitude, the envelope, or the power of signals in the time or frequency domains. Although there are more

sophisticated trigger methods than the short-time average/long-time average (STA/LTA) technique (Allen 1978), they usually require complicated parameter adjustment operations. Therefore, the STA/LTA remains the most popular method in which the ratio of average energy in a short-term window and a long-term window (STA/LTA ratio) is used as a criterion for picking. However, this method has also its own disadvantages. It requires careful setting of parameters (Trnkoczy 2002) including two window lengths and signal-to-noise ratio (SNR) threshold. A high threshold may lead to missing weak events while a low threshold can result in many false triggers.

A common shortcoming among various event detection algorithms is that they are very sensitive to the SNR level so that weak events whose energies and amplitudes are comparable to background noise may not be triggered. In other words, weak events may be obscured in the presence of strong noise. There are many sources of noise. They could be generated either naturally or artificially. The natural sources include oceans, high waterfalls, rivers, lakes, etc., while artificial sources are industrial machinery, railways, highway traffic, buildings, etc. (Nofal *et al*. 2004).

Another important source of noise other than site noise is instrumental self-noise. Self-noise of an instrument is the noise that is introduced and recorded by the equipment system itself even if there is no external source of noise. Both sensor and the digitizer of a seismograph system have their own self-noise (Ackerley & Spriggs 2012). Instrument self-noise can act as a major constraint for detection of microseismic events and analysis of ambient seismic noise in quiet environments because these signals can easily be masked in the presence of strong instrument self-noise. Therefore, it is crucial to know the instrument self-noise level before any analysis and interpretation. Lack of a self-noise standard makes it difficult to assess when a sensor's self-noise is above the manufacturers' specifications, indicating a possible problem with the sensor or noisy site conditions (Ringler & Hutt 2010).

With this in mind, we have studied microseismic data recorded using modified 4.5-Hz geophones deployed in a borehole to monitor a hydraulic fracture treatment over a shale-gas reservoir. These geophones have significantly better noise performance (higher sensitivities and lower minimum magnitude detection threshold) than that of standard 15-Hz sensors. However, we suggest that because the levels of ambient noise, which can be considered as being mostly surface waves, are very low in deep boreholes due to the distance from the surface, a comparatively large instrument self-noise can prevent detection of weak events with negative magnitudes, especially at viewing offsets in excess of 500 m. However, the decay of the surface noise is frequency-dependent (Carter *et al*. 1991; Stephen *et al*. 1994) and some frequency bands may still have energies above the instrument self-noise level.

The method used to calculate instrument self-noise is based on power spectral density (PSD) estimations. We analyse the temporal changes in recorded noise levels and their time-frequency variations using a modified Welch transform. In order to show the effects of measurement depth and instrument self-noise we compare the calculated PSDs and energy variations of the borehole recordings with those of surface broad-band seismometers in this study. We then describe how this comparison could add to the ongoing discussions about surface versus borehole microseismic monitoring (Maxwell *et al*. 2012; Eisner *et al*. 2013). Finally, we describe how variations from known background noise levels can be used for semi-automated event detection without prior knowledge of signal frequency contents. This algorithm is then compared with the typical STA/LTA technique.

2 ROLLA MICROSEISMIC EXPERIMENT

The microseismic data used for this study are from a borehole array consisting of six three-component low-frequency (4.5-Hz) receivers deployed in a slightly deviated (<20 degrees) monitoring well (well E in Fig. 1) and also from surface three-component broad-band seismometers measured during the Rolla Microseismic Experiment (Eaton *et al*. 2013). The sampling intervals of the borehole receivers and surface seismometers are 0.5 and 2 ms, respectively. The experiment recorded a multistage (21 stages) hydraulic fracture stimulation of a Montney gas reservoir in northeastern British Columbia, Canada.

The overall layout of field equipment, relative locations of the two treatment wells H_1 and H_2, a cross-section through the borehole array, and configuration of a broad-band array are shown in Figs 1(a)–(d), respectively. The shallowest borehole receiver is located at a true vertical depth of 1668 m with the other receivers positioned at 32 m spacing.

Broad-band sensors are deployed either as part of four mini-arrays consisting of four three-component seismometers (A-D) or as single three-component seismometers (F and G). 10 stages of fracture treatments took place in well H_1 during August 15–18 and 11 stages in well H_2 during August 21–25 in 2011. The broad-band seismograph units recorded data continuously while the downhole toolstring was deployed twice, successfully recording both sets of fracs. Only the borehole recordings and surface recordings at seismometers F and A_3 from the treatments at well H_2 are used for this study.

Perforation shots were fired at 200 m spacing along the horizontal component of the well H_2 and used for velocity model calibration. The true vertical depths of the perforation shots range from 1946 to 1954 m. Source-to-borehole receivers offsets for the perforation shots vary from 756.9 to 2018.8 m which are significantly larger than in typical borehole hydrofracture monitoring. Generally, the maximum distance at which microseismic events can accurately be detected depends on size of the events, attenuation, and noise level at monitoring well (Warpinski *et al*. 2009). However, the viewing distances are typically set to be below 800–1000 m (Warpinski *et al*. 2009; Maxwell *et al*. 2010).

3 EVALUATION OF ENERGY VARIATIONS

3.1 Observations

A considerable increase in energy levels is anticipated during hydraulic fracture treatments. Energy fluctuations are likely to follow injection strategies with observed seismic energy proportional to fluid injection rates for receivers situated close to the injection wells. Alternatively, energy levels may be in-line with fluctuations in ambient noise levels, e.g. due to anthropogenic activities, if receivers are placed closer to the surface. Fig. 2(a) shows the pump curves (treatment pressure, slurry rate, and blender density) for the fourth stage of the fracture treatment. The corresponding time-series for the vertical and two horizontal components in the shallowest borehole receiver are also plotted. The vertical component has higher amplitudes than the horizontal ones. The time-series are constructed by combining positive values from high-pass filtered traces (>200 Hz) with negative values from low-pass filtered traces (<50 Hz). Amplitudes of low-pass filtered traces are multiplied by 8 for the purpose of representation. Trace amplitudes do not increase significantly during fluid injection. There is only some correlation
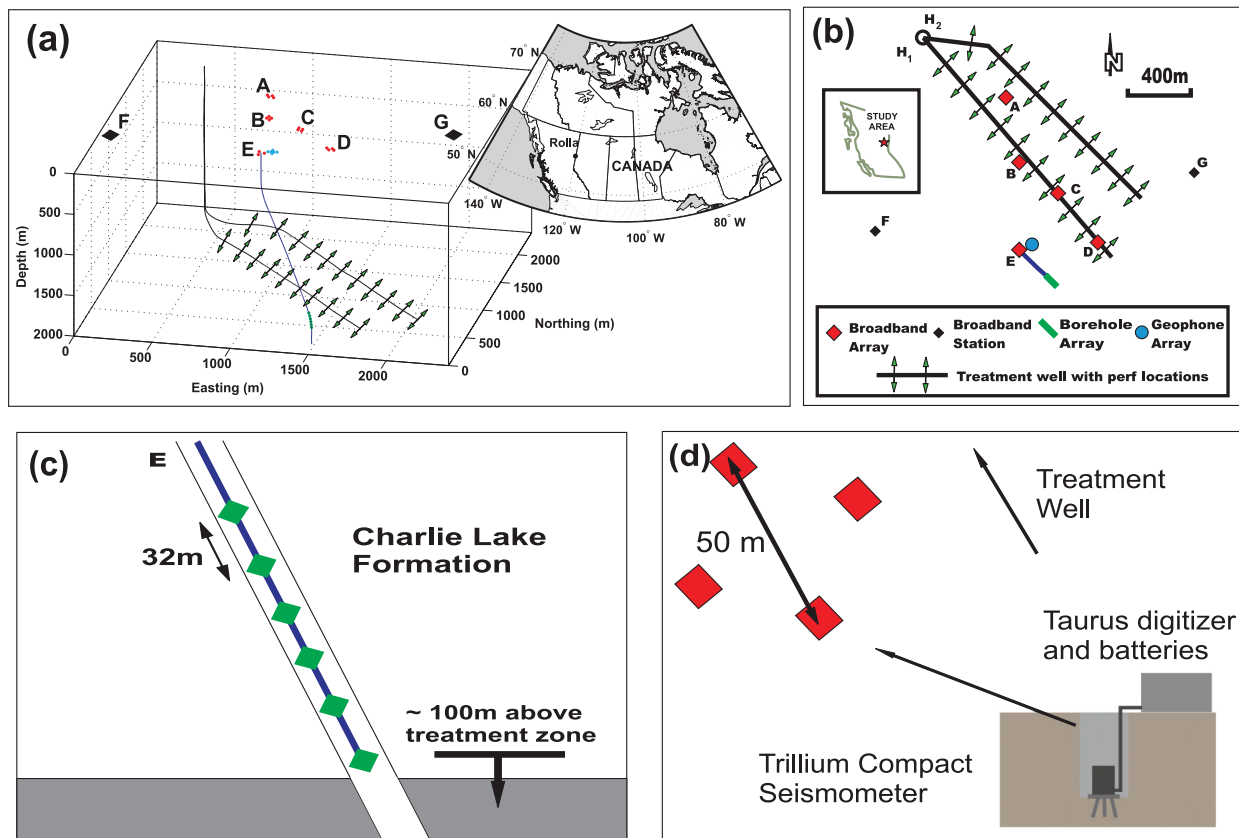
Figure 1. (a) 3-D view and (b) map view of the acquisition geometry of the Rolla microseismic experiment. Three types of microseismic recording systems were used; a borehole toolstring (E), a set of broad-band seismograph systems deployed within four-station arrays (A, B, C and D) or as individual stations (F and G), and a 12-channel array of geophones located near the borehole system. H_1 and H_2 are the injection wells. (c) Cross-section showing borehole toolstring of six 3-C geophones (modified after Eaton *et al.* 2013). (d) Configuration of surface broad-band seismometers. Each array consists of four stations forming a diamond shape pointing at the injection well head.

between slurry rate and the vertical component amplitudes for frequencies less than 50 Hz. The period jumps in signal strength on the horizontal components are thought to be electronics-related and discarded in our following analyses. The time-series at broad-band surface seismometers A_3 and F corresponding to the same hydraulic fracturing stage are also shown in Figs 2(b) and (c), respectively. At the surface, the horizontal components have higher amplitudes than the vertical ones. Contrary to the borehole receivers, surface seismometers display various amplitude increases associated with fluid injection.

In Fig. 3(a), temporal variations in recorded energy are plotted for all three components of the shallowest borehole receiver. The energies are computed for individual 20-min long windows of data overlapping by 50 per cent and attributed to the time at the centre of the windows. Energies are displayed on a logarithmic scale. The blue dashed line represents the time when the fourth stage of treatment takes place. The red dashed lines identify the times of all other treatment stages. No significant energy variations are observed over the entire measurement period. Furthermore, there is no notable energy increase corresponding to treatment times except for stage 1. For comparison, the temporal energy variations are also computed for surface broad-band seismometers A_3 and F and displayed in Figs 3(b) and (c), respectively. As expected, the background noise energy levels are much higher on surface records than on the borehole receivers. On the other hand, more energy variations are observed at the surface during the recording time.

Fig. 3(d) shows the recorded energies at seismometer F for corresponding time-series high-passed above 0.7 Hz. The diurnal energy variations are now much more evident than in Fig. 3(c) meaning that frequencies below 0.7 are contributing predominantly to the total energy in Fig. 3(c).

3.2 Interpretation

Generally, when recording the ambient background noise for a long period of time (days or more), a diurnal energy trend is observed with higher energy at daytime than night time (Bonnefoy-Claudet *et al.* 2006). Fig. 3(a) shows no diurnal energy variations or any kind of periodicity in the recorded energy but an essentially constant level. This is the case for all other borehole receivers too.

Ambient noise, which is considered as mostly comprised of surface waves, becomes weaker with depth (Carter *et al.* 1991; Stephen *et al.* 1994) due to diminishing noise sources, for example anthropogenic noise is predominantly generated at the surface. This fact can also be inferred from comparing energy levels at surface seismometers and borehole receivers displayed in Fig. 3. The rate of decay in ambient noise level with depth is site and frequency dependent. Generally reduction in noise amplitudes at high frequencies is much higher than for low frequencies. For instance, Carter *et al.* (1991) have reported that noise levels in their study area between 15 and 40 Hz are more than 10 dB less at 945 m depth than at the surface, and from 40 to 100 Hz the difference is more than 20 dB.
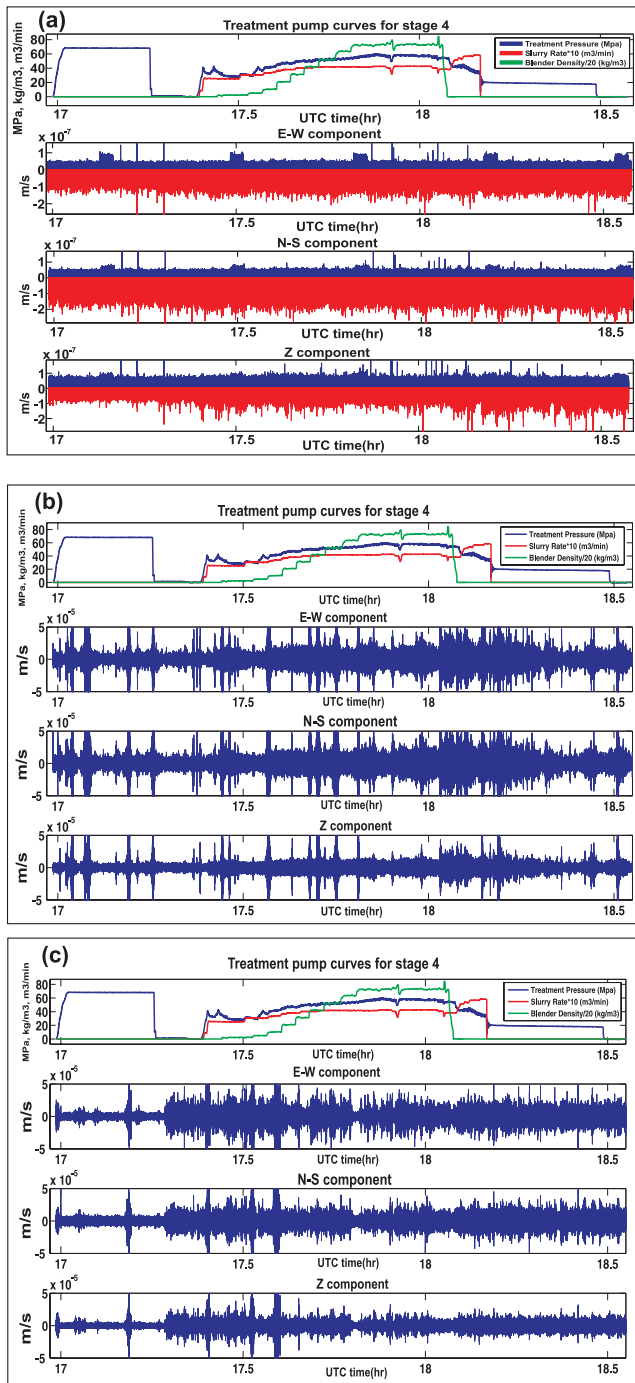
Figure 2. (a) The pump curves for proppant (green), slurry (red) and pressure (blue) rates for the fourth stage of the treatment in well H_2 along with the corresponding vertical and two horizontal component recordings at the shallowest receiver, respectively. Positive values represent high-passed filtered trace (>200 Hz) while negative values show low-pass filtered traces (<50 Hz). Time axis is in Universal time (UTC). No significant energy increase corresponding to treatment time is observed, except for the low-frequency part of the vertical component. (b) and (c) The pump curves for the fourth treatment stage along with the corresponding horizontal and vertical component time-series at the surface seismometers A_3 and F, respectively. The recorded energy increases during the treatment times.

The lack of any diurnal energy trend in our borehole data set can be attributed therefore to the depth of the experiment (1668–1828 m). The observation of diurnal energy variations at surface (Fig. 3) favours this idea. However, the depth cannot justify lack of energy bursts caused by injection of large volumes of fluids in the borehole recordings. Furthermore, if depth was the sole reason, no energy increase associated with fluid injection should have been observed for the surface recordings either, which is not the case as shown in Figs 2(b) and (c).

Constant noise levels for borehole sensors, however, can be justified assuming the background noise level is below the instrument self-noise. In addition, lack of correlation between variations in recorded energy and treatment times, except possibly for the first and closest stage, can also be justified if instrument self-noise averaged over all frequencies overwhelms the coherent signals emitted during hydraulic fracturing due to the distance of injection well H_2 from the observation well (Fig. 1). The source of instrument noise can be either thermal noise in the geophone itself, Johnson noise, voltage, and current noise in the preamplifier, or digitizer noise (Riedesel *et al*. 1990). Obviously the large time window (20 min) implies that individual microseismic events are less likely to dominate average energy computations, as individual coherent events including perforation shots have been recorded. Likewise, the energy of low-pass filtered recordings shows a clearer correlation with injection rates (Fig. 2a). Therefore individual frequency bands may still contain coherent energy above the instrument self-noise level in this experiment. Nonetheless, a clear understanding of instrument self-noise levels is an important factor in microseismic analyses.

4 INSTRUMENT SELF-NOISE ESTIMATION

In the previous section we described how self-noise of the recording instrument obscures background noise and also signal and noise energy variations for deep deployments more than 700 m away from the injection stages and may consequently complicate the interpretability of data. It may bury small microseismic events rendering their detection and make time picking challenging. Only strong events whose energies are above the self-noise can then easily be detected. In this section, we analyse the recorded energy levels as a function of frequency.

4.1 Method

The different methods available to estimate self-noise of sensors make side-by-side comparisons of their performance difficult (Hutt *et al*. 2009). We use PSD estimates to obtain the self-noise assuming a stationary background noise. Calculating the noise PSD is a common method for quantifying seismic background noise. We compute the average PSDs of the entire data for each component and consider them as the upper bound of the instrument noise floor. Power spectra are computed using the Fourier transform and a modified Welch method (Welch 1967) as outlined by McNamara & Buland (2004) using Hanning window tapers of 20-s and 400-s length for borehole sensors and surface seismometers, respectively, with 50 per cent overlap. By removing the energetic events, transients, and any types of noise bursts, we consider only the noise at quiet times to calculate the PSDs (Peterson 1993). The calculated individual PSDs are transformed into dB and averaged over the number of windows to obtain the average PSD for each component. The 1st, 5th, 25th, 50th, 75th, 95th and 99th percentiles (Berger *et al*. 2004)
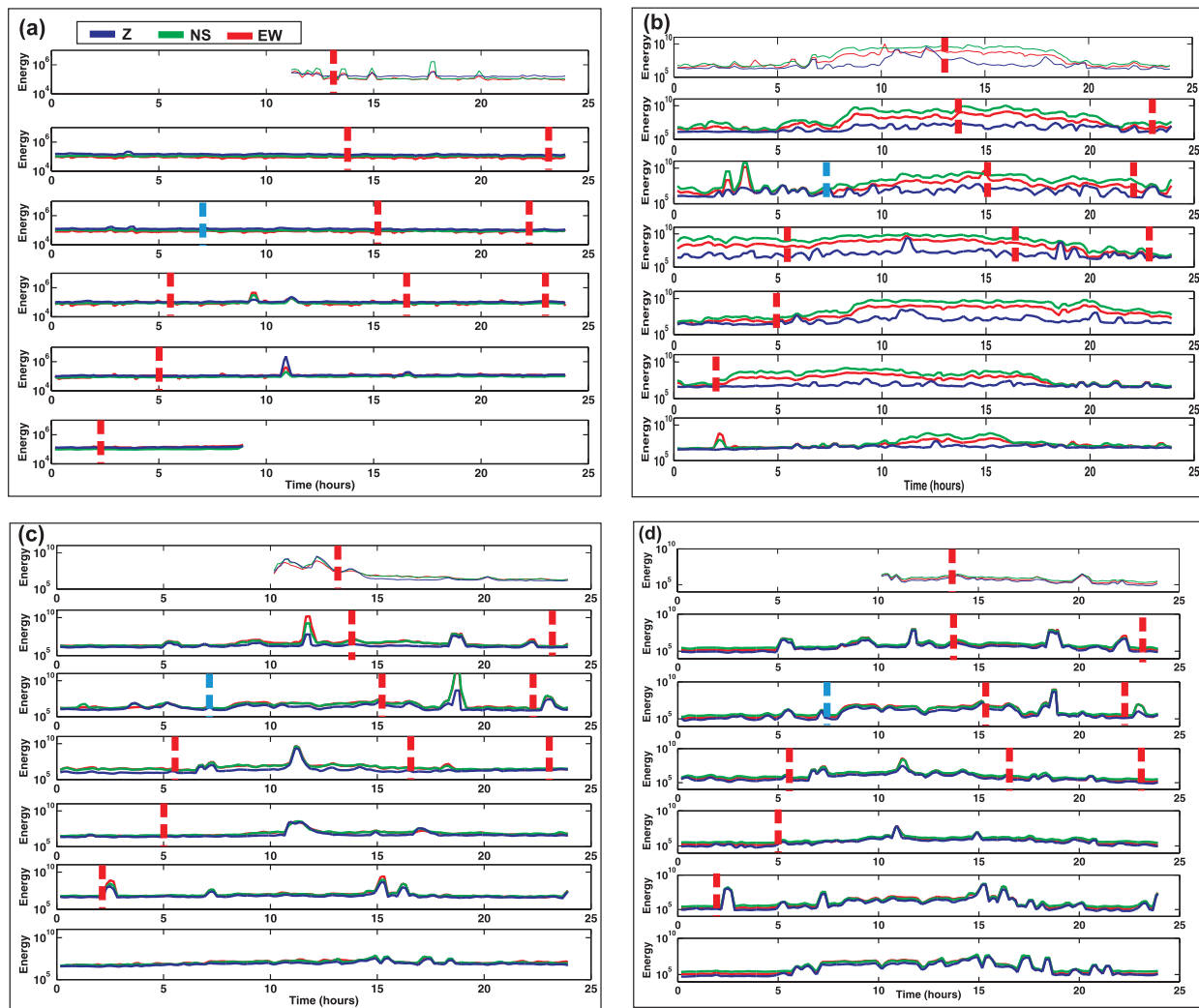
Figure 3. (a) Energy variations over the entire treatment period at well H_2 for the shallowest borehole receiver. Red, green and blue correspond to the E–W, N–S and vertical (Z) components, respectively. Blue dashed line denotes the time at which the fourth treatment stage starts and red dashed lines show the start time of all the other stages. Recorded energy is mostly constant and shows little to no correlation with injection times nor any diurnal variations. (b) and (c) The same for surface seismometers A_3 and F, respectively. Energy variations associated with diurnal energy variations plus treatments are observed, especially for A_3. (d) Similar to (c) but for time-series high-passed above 0.7 Hz. The energy variations are more evident.

are also calculated for the transformed PSDs to provide a better understanding of their statistical variations at different frequencies and more insight in stationary (or non-stationary) constituents of the ambient noise field. Moreover, the percentiles can be used to estimate the probability of detecting a microseismic event (Goertz *et al.* 2012).

4.2 Results

The estimated average and percentile PSDs for all three components of the first and the fifth borehole sensors (counted from the top) and surface broad-band seismometers A_3 and F are shown in Figs 4 and 5, respectively. The Peterson's high noise model (HNM) and low noise model (LNM) have been plotted for comparison. In Fig. 4, the blue dashed line represents the self-noise model of a conventional 15-Hz sensor while the green-dashed line represents the manufacturer's self-noise model for the 4.5-Hz instruments used in this study (Goertz *et al.* 2011). The manufacturer's self-noise model for the broad-band seismometers are plotted as blue dashed lines in Fig. 5. The subtle peaks in all spectra at frequency of 0.2–0.3 Hz

represents the ocean microseism generated primarily by the wave–wave interaction beneath storms over the ocean (Lee 1935; Ewing *et al.* 1957).

The modified borehole instruments in this experiment have higher sensitivity and lower detection thresholds than the common 15-Hz sensors, with sensitivities close to the Peterson's low-noise model for surface recordings. Since the averaged PSDs have been computed for quiet times, we consider them as the detection threshold at each receiver. The flat PSD curve bottoms in the interval of 30–200 Hz in Fig. 4 suggest that the detection threshold in this frequency range may have been reached, especially for receiver 5, and the instrument self-noise could be what is recorded dominantly. This threshold is around –195 dB. This is somewhat higher than the published instrument self-noise level (green line) but still significantly better than a 15-Hz geophone (blue line). Nonetheless, any event without significant energy beyond this threshold will be difficult to detect on the recordings. This will be explored in more detail in the next section.

Comparing the statistical distribution of percentile curves at different frequencies in Fig. 4 shows that their shapes vary only slightly,
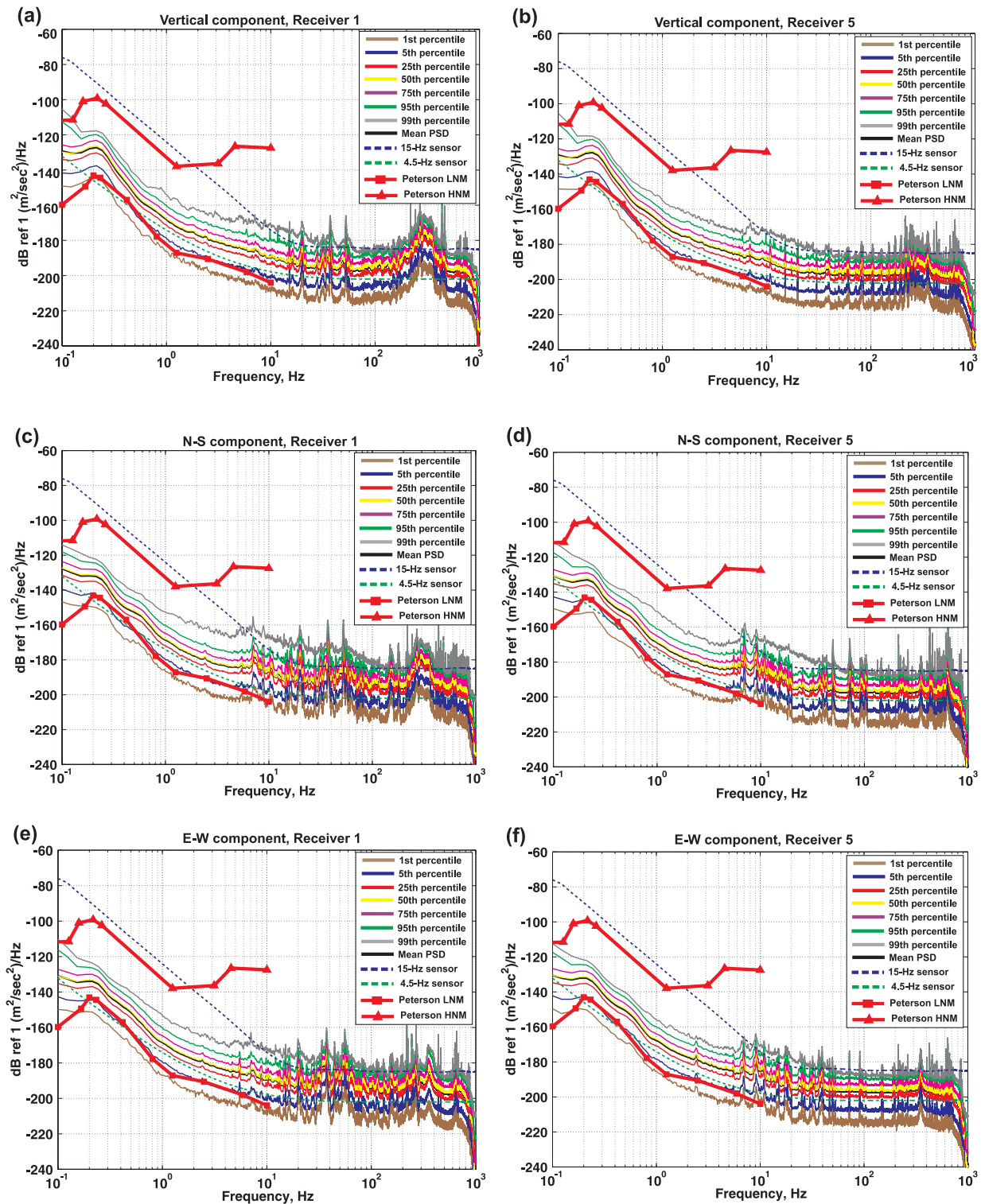
Figure 4. (a), (c) and (e) The average PSD plus 1st, 5th, 25th, 50th, 75th, 95th and 99th PSD percentile estimates for the vertical and two horizontal components at borehole receiver 1 (counted from the top), respectively, as a function of frequency. (b), (d) and (f) The same for receiver 5. The solid black curves demonstrate estimated average PSD. Upper and lower red curves show Peterson's low noise and high noise models, respectively. The blue dashed line represents the self-noise model of a conventional 15-Hz sensor while the green-dashed line represents the manufacturer's self-noise model for the 4.5-Hz instruments used in this study. Estimated PSDs are above the manufacturer's specification but lower than for a 15 Hz geophone.

justifying the assumption of a stationary background noise model. Comparing Figs 4 and 5 shows that background noise levels are much higher at the surface by 30–40 dB at 10 Hz, and exceed the instrument self-noise level at all frequencies below 30 Hz. The sur-

face PSD curves closely follow the trends of the Peterson's noise models and nearly all percentiles are contained within the high-and low-noise platforms. Surface PSD percentile curves display a larger variety of shapes and span a larger magnitude range than the
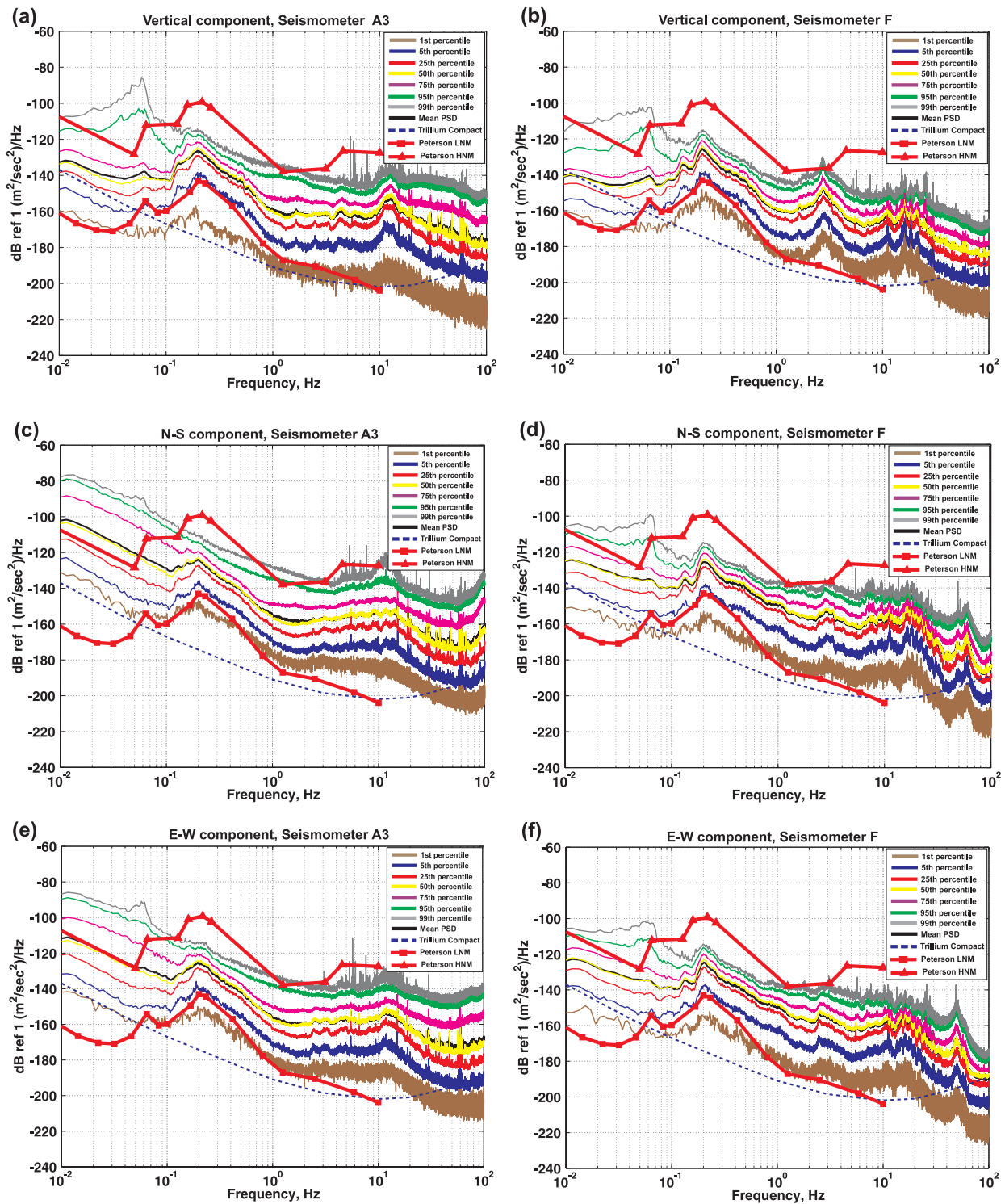
Figure 5. (a), (c) and (e) The average PSD plus 1st, 5th, 25th, 50th, 75th, 95th and 99th PSD percentile estimates for the vertical and two horizontal components at surface seismometers A₃, respectively, as a function of frequency. (b), (d) and (f) The same for seismometer F. The solid black curves demonstrate estimated average PSD. Upper and lower red curves show Peterson's low noise and high noise models, respectively. The blue dashed line represents the self-noise model of the seismometers. The noise power levels are well above the estimated self-noise model and also higher than in borehole receivers.

corresponding borehole PSD curves. This implies a larger noise variability at the surface, and may also be indicative of a larger degree of non-stationarity in the surface noise.

To check if the frequency plateau between 30 and 200 Hz in Fig. 4 is indeed close to the self-noise level of the borehole instruments,

we compute averaged time-frequency spectrograms in a similar way as before. Fig. 6(a) shows the variation of PSDs over time for the vertical component of the shallowest borehole receiver. The PSDs are averaged for each hour of recording and plotted versus time in this figure. The color bar specifies the power values. Fig. 6(b) zooms
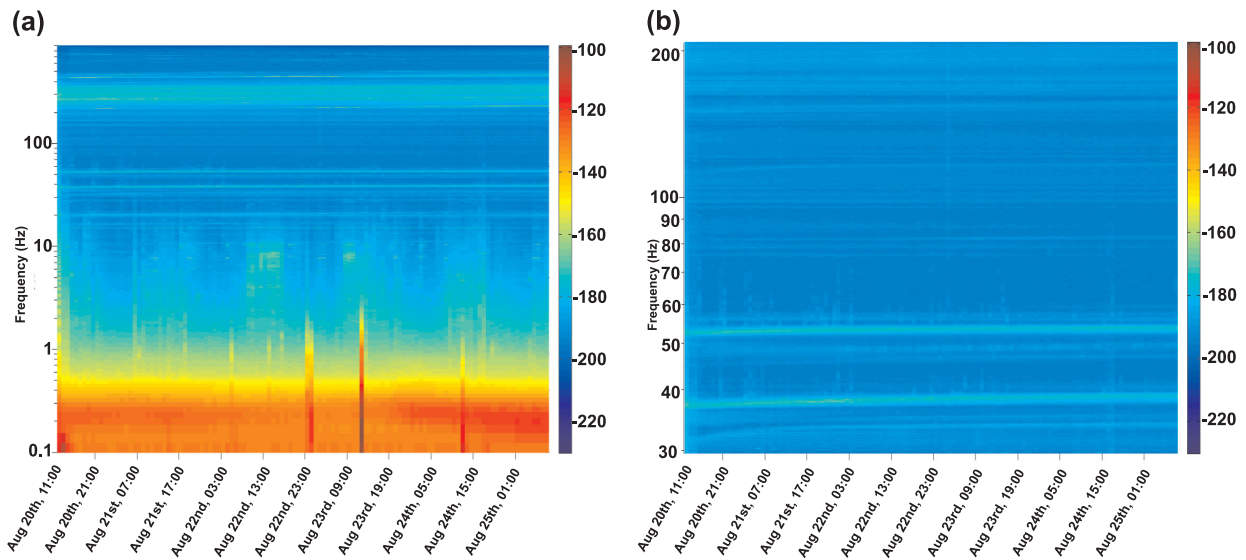
(a)

(b)

Figure 6. (a) The time-frequency representation of PSD variations for the vertical component of the shallowest borehole receiver. (b) Zoom in for the frequency range of 30–200 Hz only. Energy levels are approximately constant except possibly between 1 and 15 Hz.
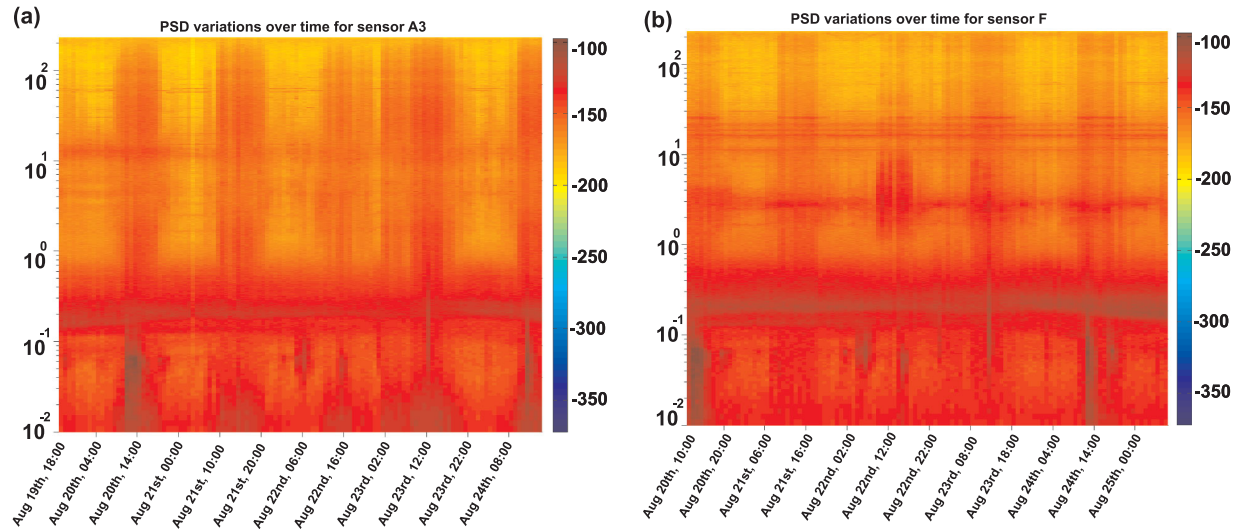
(a)

(b)

Figure 7. (a) and (b) The time-frequency representation of PSD variations for the vertical component of the surface seismometers A_3 and F, respectively. The diurnal energy variations exist in most of the bandwidth.

in on the frequency range of 30–200 Hz. No significant changes in the power levels are visible except between 1 and 15 Hz. The latter have a diurnal time period and are likely related to anthropogenic or ambient noise from the surface. The absence of significant energy fluctuations for all other frequencies confirms our hypothesis that the plateau is indeed indicative of the instrument self-noise level. For comparison purpose, the averaged time-frequency spectrograms for surface seismometers A_3 and F are displayed in Figs 7(a) and (b), respectively. The diurnal energy variations are evident in these figures for most of the frequency bandwidth as opposed to Fig. 6(a).

4.3 Implications

The minimum magnitude detection threshold increases with distance from the observation well (Fig. 8a). One view is that this is due to attenuation of signal energy with increasing distance combined with high ambient noise levels. Ambient noise levels decrease however with depth. Therefore in deep wells, the instrument noise

level may well be the limiting factor for event detection. Fig. 8(a) also shows that the minimum detection threshold for a 4.5-Hz sensor (blue curve) is 0.5 magnitude unit improved with respect to that of the 15-Hz seismometer (red curve). Figs 8(b) and (c) show source spectra for five events of different magnitudes between –3 and –1 at 0.5 magnitude steps for source–receiver distances of 200 and 1200 m, respectively, together with the manufacturer's self-noise estimates of the used tool, a standard 15-Hz tool, and the Peterson's reference noise models (Goertz *et al.* 2012). A quality factor of 150, a generic stress drop of 1 MPa, and shear velocities of 3400 m s^{-1} at the source and 3060 m s^{-1} at the receiver are assumed (Goertz *et al.* 2011). For a source–receiver distance as large as 1200 m, the detection threshold of the modified 4.5-Hz geophones is approximately $M_W = -1.5$, about 1/2 magnitude unit better than a conventional tool. This can be translated into detection of nearly three times more events (Goertz *et al.* 2011).

In the Rolla microseismic experiment we are dealing with distances to the perforation shots in excess of 700 m for well
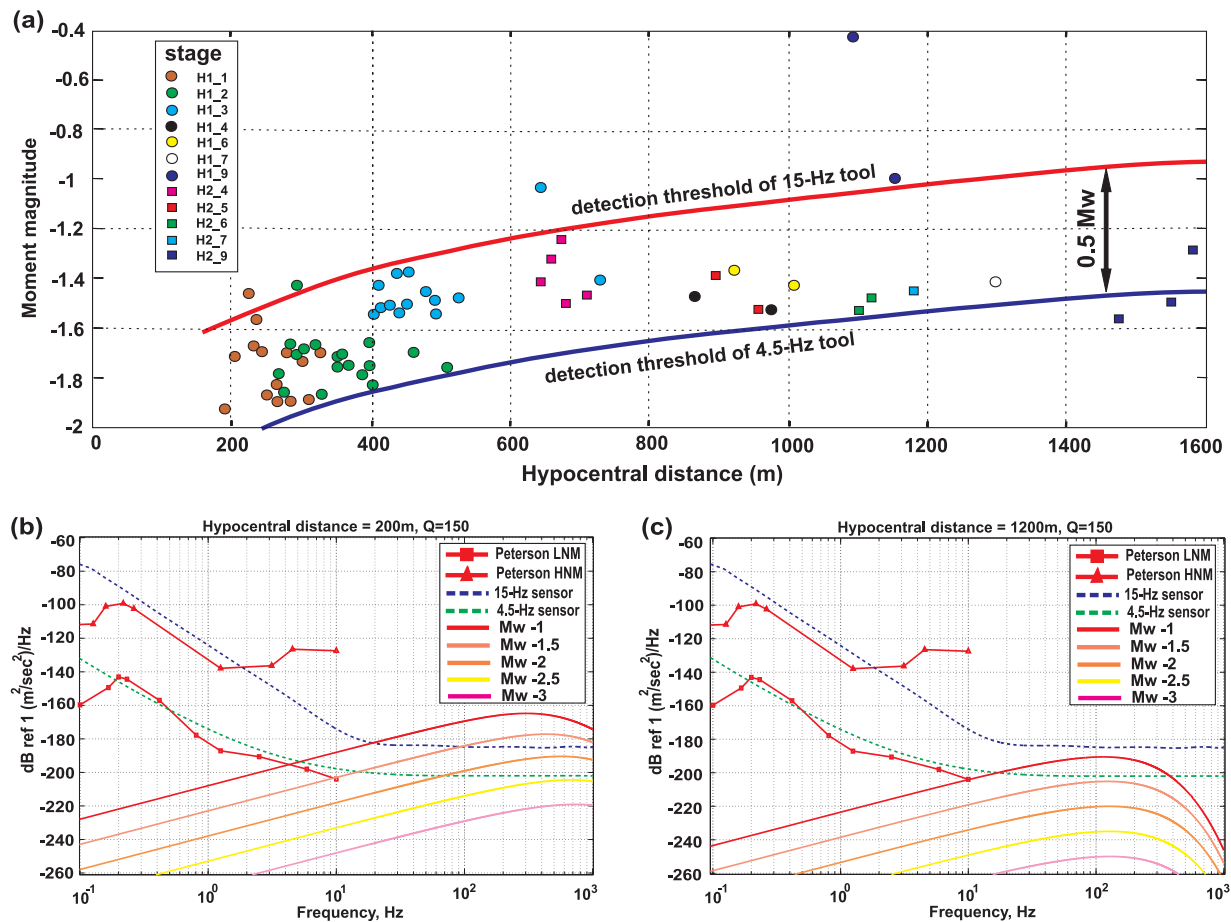
Figure 8. (a) Minimum magnitude detection threshold increases with distance from the observation well. Sensitive tools can lower the threshold leading to detection of more weak events (modified after Eaton *et al.* 2013; Goertz *et al.*, personal communication, 2012). (b) and (c) Source spectra for events of different magnitudes for source-receiver distance of 200 and 1200 m, respectively, assuming $Q = 150$. Contrary to the 15-Hz geophones, the 4.5-Hz receivers can still detect events of magnitude around −1.5 for the distance of 1200 m.

H_2 (Fig. 1), thereby significantly reducing the minimum anticipated magnitude detection threshold. Nonetheless, a reduced instrument self-noise level in this quiet environment clearly allows for reduction of the magnitude detection thresholds with distance (Fig. 8). Therefore we might be able to reduce magnitude detection thresholds with distance (Figs 8a and b). This may lead not only to more useful events but also aids in multi-well recordings where many events are solely detected on a single well.

Our observations also have implications for ambient noise tomography using seismic interferometry in order to obtain a velocity model and reveal the subsurface structure nearby the wellbore (Miyazawa *et al.* 2008; Grechka & Zhao 2012). This method aims at recovering the Green's function between two receivers by cross-correlating passive seismic recordings, thereby emphasizing coherent features in an apparent random ambient noise field. After removing the mean and dc trend from 1-hr long data windows from borehole recordings, the data are fragmented into individual 15-s segments. In order to calculate the average cross-correlation functions between the shallowest receiver and each of the other receivers the signs (1-bit form) of corresponding individual pre-whitened segments are correlated and then stacked (Larose *et al.* 2004; Bensen *et al.* 2007).

Fig. 9(a) demonstrates the obtained result for the vertical component after applying a bandpass filter with corner frequencies of [180 200 400 440] Hz. It is related to a causal coherent signal travelling from the shallowest receiver, acting as a virtual source (Bakulin & Calvert 2004), down the array to the deepest receiver. The moveout velocity of about 1500 m s^{-1} calculated from the red dashed line suggests that these high amplitude features are actually related to tube waves propagating within the fluid and along the wellbore. Unfortunately tube waves hold little information about the subsurface beyond the immediate borehole vicinity and are therefore less useful for analysing, for instance, temporal variations in the Earth due to fluid injection.

Fig. 6(a), however, shows some diurnal variations in the recorded powers at the low frequency range of 1–15 Hz. Fig. 9(b) shows the crosscorrelation functions for this frequency range. A best-fitting line through the maximum correlation values shows an apparent velocity of 6200 m s^{-1}. Based on the sonic velocity log shown in Fig. 9(c), these waveforms can be attributed to a high-amplitude low-frequency *P*-wave originated from the surface and travelling down the borehole array. This *P*-wave may have been caused by either a low-frequency noise source at the surface or conversion of anthropogenic surface waves to waves travelling along the borehole. At first sight the recovered *P*-wave moveout seems high. The Charlie Lake formation (where the borehole sensors are sitting) is however composed of large bodies of anhydrites, limestone, and dolomite which can increase the *P*-wave velocities quite significantly (Edwards *et al.* 2012).
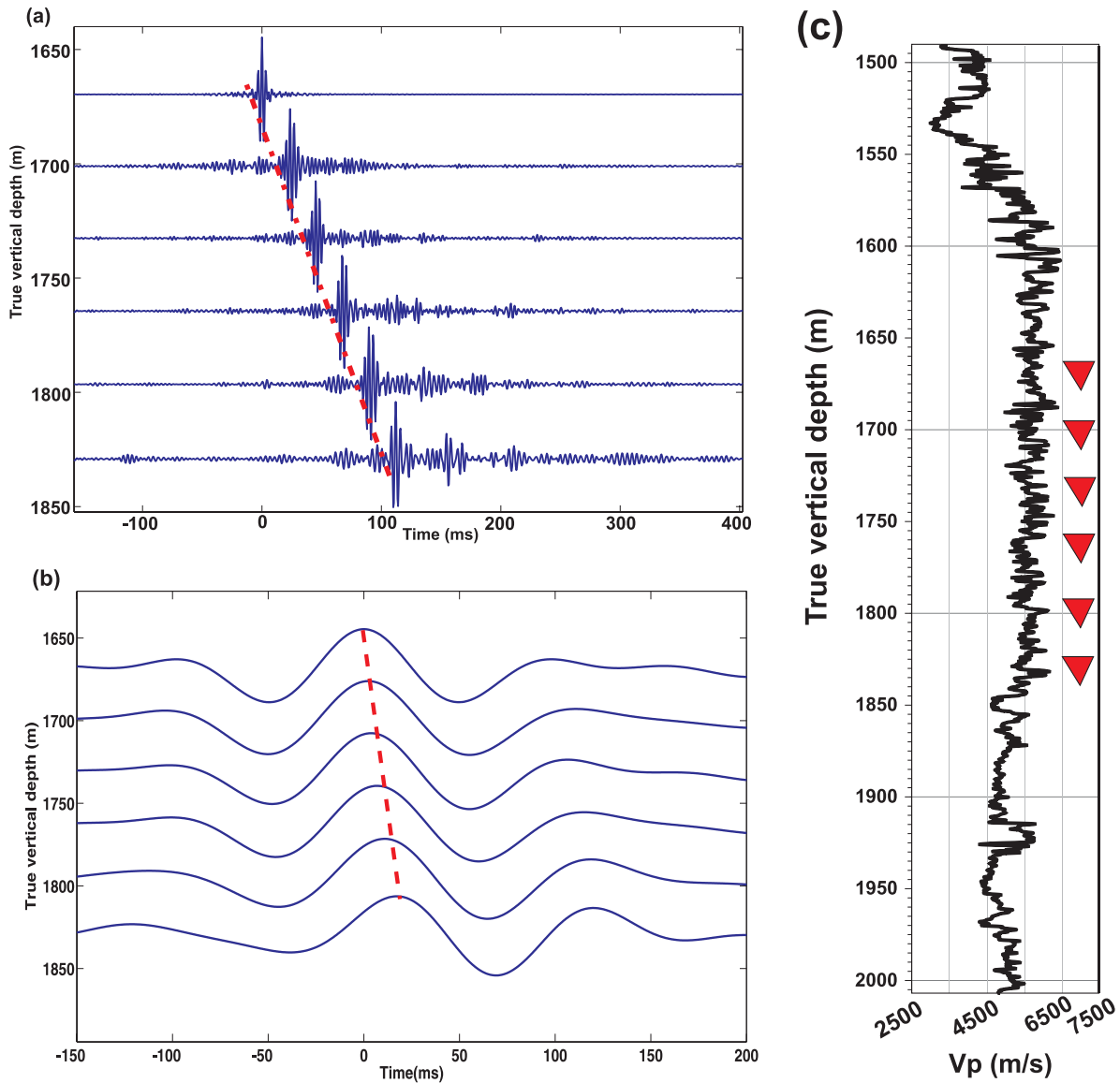
Figure 9. The averaged cross-correlation functions between the vertical component of the shallowest receiver and all other receivers in the borehole array after a bandpass with corner frequencies of [180 200 400 440] Hz. The move-out velocity of the reconstructed coherent and high-amplitude waveforms is approximately 1500 m s^{-1}. This suggests that these waveforms are most probably tube-waves propagating down the array and within the borehole fluid. (b) Corresponding result for frequencies of [1 5 10 15] Hz. The moveout velocity is 6200 m s^{-1}. (c) The sonic velocity log for *P* waves. The high velocities suggest that the waveforms in (b) may represent a *P*-wave travelling down the array.

We suggest that the inability to recover the weaker coherent signals corresponding to *P* and *S* waves along the borehole is due to the relatively high level of instrument self-noise with respect to the background noise. Therefore, analysis of coherent ambient noise using seismic interferometry can be challenged by dominant instrument self-noise in deep environments.

5 A NEW METHOD FOR MICROSEISMIC EVENT DETECTION AND TIME PICKING

Our PSD analysis method can also be used as an event detection algorithm by computing the average PSD for the entire record and the standard deviations for the individual frequencies. Any short time segments with a PSD that is statistically larger than the average

PSD by some likelihood threshold is then a potential event. This method can also indicate which individual frequency bands are statistically above the average threshold. This may be useful in determining suitable bandpass filters.

An example is shown below to demonstrate our proposed detection algorithm. The inset in Fig. 10 displays four microseismic events (B_1, B_2, B_3 and B_4) appearing at short time intervals right after the fourth treatment stage at the shallowest borehole receiver. This figure also shows the computed average PSD and its standard deviations at each frequency, as well as the PSDs for the four microseismic events and two noise recordings. A window length of 0.25 s is chosen so that sufficient temporal and spectral resolutions in the time-frequency representations are provided. All event PSDs exceed the average PSD, especially at the frequency range of 25–430 Hz. Also the PSDs of two segments just before event B_1 and after event B_4, which consist of background noise only, have been
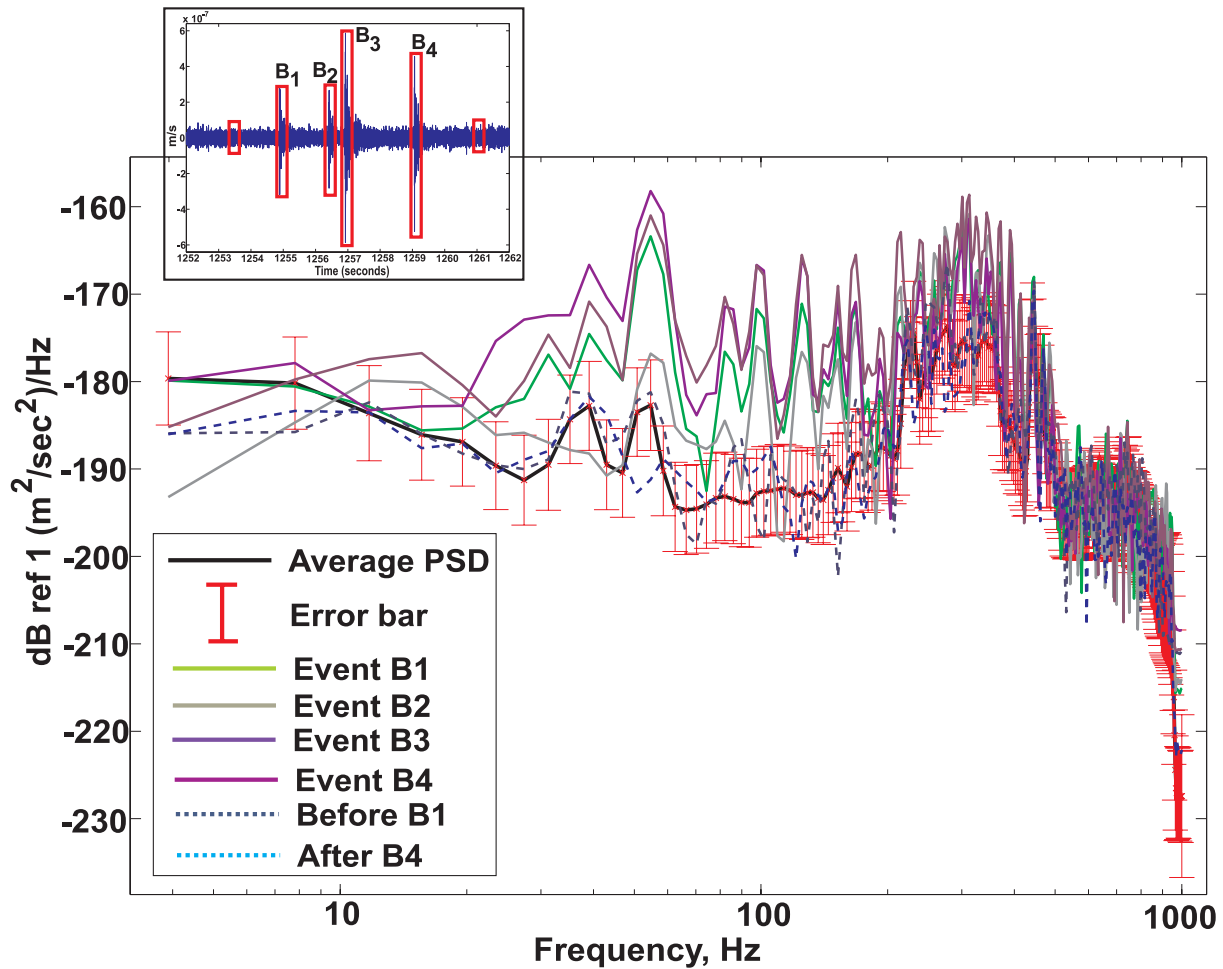
Figure 10. Four microseismic events (B_1 to B_4) during the fourth treatment stage recorded on shallowest borehole receiver with red boxes showing analysed microseismic and noise recordings (top inset), PSD estimates for all four events (continuous coloured line) and the averaged PSD (black line) including frequency-dependent standard deviations. The dashed lines correspond to PSD of segments just before B_1 and after B_4.

plotted (dashed lines in Fig. 10) to show that the noise PSD lies mostly within one standard deviation.

In the next step, a rolling window of length 0.25 s is used and the PSD is computed for each segment throughout the data. The average PSD is then subtracted from all individual PSDs:

$$misfit_t(f) = PSD_t^i(f) - \overline{PSD}(f), \tag{1}$$

where $misfit_t(f)$ stands for the PSD difference at each time t as a function of frequency f, $PSD_t^i(f)$ denotes the individual PSD at the corresponding time, and $\overline{PSD}(f)$ is the calculated average PSD. These differences are then divided by standard deviations at each frequency as following:

$$y_t(f) = \frac{misfit_t(f)}{std(f)}, \tag{2}$$

where $std(f)$ is the standard deviation at frequency of f Hz. The resulting time-frequency representation highlights then all signals that stand out in a statistical sense from the reference spectrum, in this case the background noise.

Fig. 11(a) displays the results $y_t(f)$ in the neighbourhoods of the events B_1–B_4. The events can easily be detected as they correspond to anomalous high values over specific frequency ranges. As microseismic events are expected to be of greater powers than the background noise and most of the background noise lies within 1–2 standard deviations, only the values greater than 1 standard devia-

tion at each frequency are kept (Fig. 11b). This figure shows that the frequency band over which the events are significantly dominant with respect to the noise is 25–430 Hz. This can help in designing suitable bandpass filters in order to better identify and analyse microseismic events.

Events B_1 to B_4 have PSDs that are larger by 2–6 times the standard deviation of the noise model within this frequency range. Assuming a Gaussian probability distribution, this quantifies to probabilities only from 13.6 per cent to less than 0.01 per cent that these are due to random noise fluctuations. In order to make the onset-time picking of the events easier, the calculated quantities in Fig. 11(b) are summed over all frequencies:

$$Y(t) = \sum_{f=0}^{f_{Nyq}} y_t(f), \tag{3}$$

where $Y(t)$ is the sum as a function of time and f_{Nyq} represents the Nyquist frequency. The result in Fig. 11(c) shows how microseismic events stand out of the noise at the corresponding arrival times.

For comparison, Fig. 11(d) shows the result of STA/LTA method considering a short and a long window length of 15 and 150 ms, respectively. By setting a STA/LTA ratio threshold equal to 4 one can easily detect the events at similar times as our technique. Choosing shorter window lengths has provided a better time resolution for the STA/LTA method than our suggested method. Nonetheless, the PSD
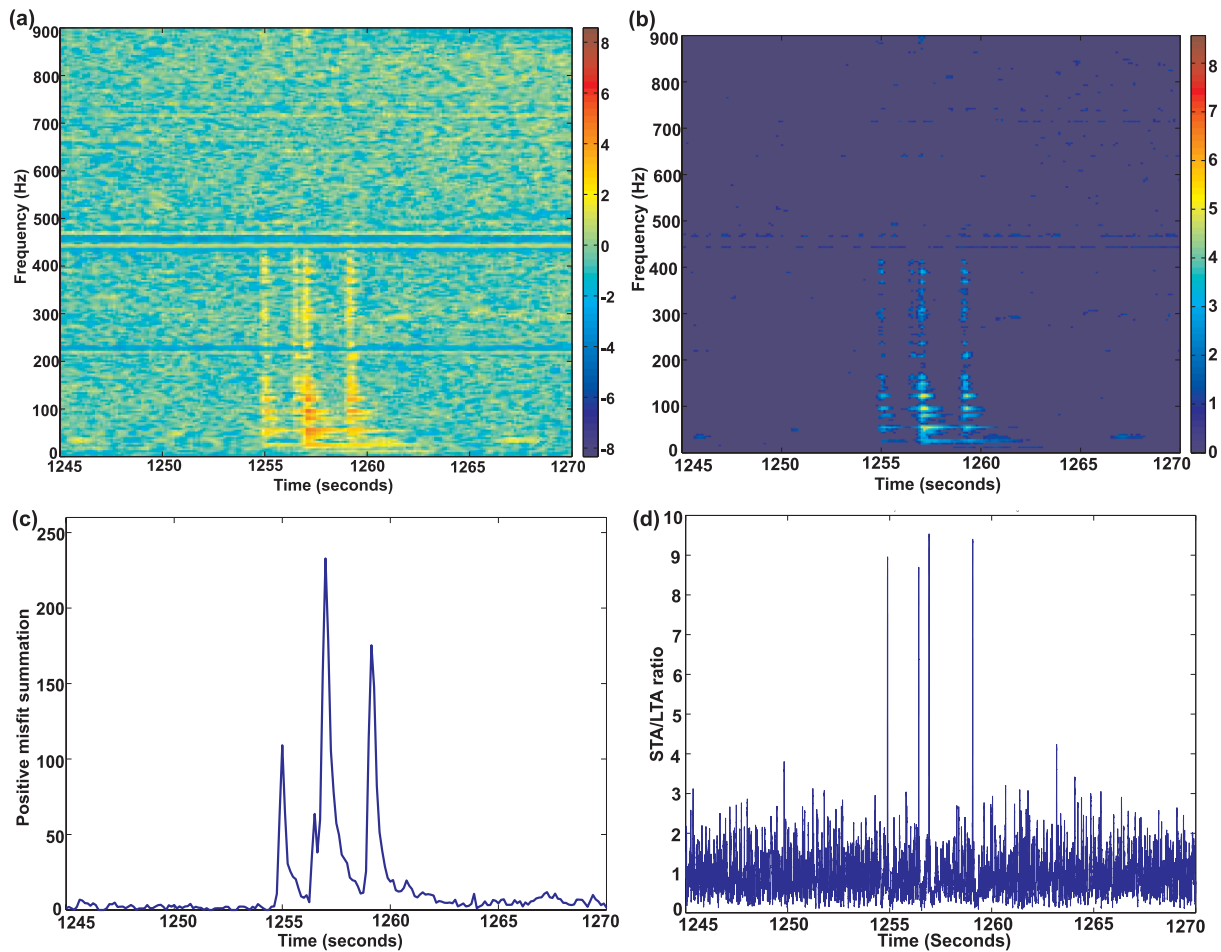
Figure 11. (a) The time-frequency representation of individual segment PSDs minus average PSD, divided by standard deviations at each frequency. (b) The same as (a) but only misfits greater than one standard deviation are kept. (c) The summation of results in (b) over all frequencies. The events can be identified by their anomalous high values. (d) The result of STA/LTA analysis showing that these events represent high ratios.

method can easily detect the presence of the coherent signals, even if the exact frequency bandwidth of the original signals is *a priori* unknown. The STA/LTA method on the other hand can more easily detect the onset of the various signals, thereby better distinguishing between arrivals B_2 and B_3 (Fig. 10) but at the expense of more variations in STA/LTA output levels even if no signals are present (Fig. 11d).

6 DISCUSSIONS

Event detection and automatic time picking is a very important step in the processing of microseismic data. The accuracy of the event location, event identification, and source mechanism analysis is very much dependent on data quality. Instrument self-noise in quiet environments or consistently high ambient noise levels can complicate event picking using the STA/LTA method. In such environments weak microseismic events will be obscured in the presence of relatively higher instrument self-noise. Therefore, compared with shallow studies, we suggest that deep borehole microseismic acquisitions require sensors of higher sensitivity and lower self-noise to be installed at offsets in excess of 1 km from the treatment area to reduce the minimum magnitude detection threshold. This will increase the probability of detecting a greater number of microseismic events and consequently more detailed interpretations.

Other than strong instrument self-noise relative to the ambient noise level, bad coupling of the borehole instruments to the well could also explain the observations for the borehole data set in the Rolla microseismic experiment. If the sensors are not well clamped to the wellbore they may mostly record the instrument self-noise. Therefore, weak events are unlikely to be detected. Although surface recordings may not suffer from instrument self-noise as much as borehole experiments do they are more affected by high levels of surface noise so that detection of weak microseismic events at the surface might be cumbersome. Waveform stacking (Shemeta *et al.* 2009; Ozbek *et al.* 2013) can be an alternative for improving the event amplitudes with respect to the ambient noise but does rely on the recorded signal amplitudes exceeding the instrument self-noise level. In other words, stacking can only retrieve weak signals if their arrivals are aligned, their waveforms are consistent, and the individual signals amplitudes are masked by ambient instead of instrument noise. Signal amplitudes below the instrument noise level are less likely to be retrieved using stacking, as instrument noise can act more as an amplitude threshold breaking the assumption of linear superposition of signal and noise required for eliminating random noise by summation. On the other hand, waveform stacking can reduce the effect of ambient noise since the recording is comprised of a linear superposition of ambient noise and desired signal, as long as both are contained within the dynamic range of the acquisition system.

This has important implications for borehole versus surface acquisition of microseismicity. Acquisition at the surface is significantly more cost effective and allows for deployment of hundreds to thousands of receivers; yet it has the disadvantage that the propagation distances from the microseismic events to the receivers are much larger, greatly reducing the number of easily detected events. Borehole deployments are significantly more expensive, generally use two to three orders less instruments but allow for detection of many more events. The larger number of surface receivers may allow for improved ambient noise reduction; yet both acquisition strategies may be limited by their instrument sensitivity, in particular if conventional 15-Hz geophones are used, and event locations are more than 1 km away from the receivers (Fig. 8).

Compared with the STA/LTA algorithm, our suggested event detection method uses a similar number of parameters, namely a detection threshold and a sliding window of pre-specified length. As the PSD technique is based on the time-frequency representations, the window size should be chosen such that it trades-off between temporal and spectral resolutions. The window length should be small enough to make closely-spaced events distinguishable and large enough to allow long-period components to be adequately accounted for in the analysis. The PSD method is devised to be insensitive to variations in signal frequency content. Conversely, it does assume constant background noise levels. It can also be used to design a more suitable bandpass filter for further analysis of microseismic data whereas the STA/LTA method usually requires the data to be bandpassed prior to event detection.

However, it should be noted that onset-time picking and event detection are two different concepts. The former includes specifying the exact arrival time of the event whereas the latter implies only the presence of events. When the parameters are best set, the STA/LTA technique seems to better determine the onset-times while the PSD method works best in identifying the presence of an event. We suggest that the PSD method would relatively do better in detection of emerging events where the gradual amplitude increase can make the STA/LTA method fail.

7 CONCLUSIONS

Considering the depth of the receivers, observation of very small to absent energy variations during the fracture treatments and fluid injections, lack of diurnal energy trend, and a constant energy level throughout the borehole data suggest that the self-noise of the instruments is a major limiting factor in deep microseismic experiments. The averaged and time-varying power spectral densities show that the instrument noise floors are being reached in this data set especially at the frequency interval of 30–200 Hz. In quiet environments, instrument self-noise may thus be the limiting factor determining the magnitude–distance detection threshold. It can also make the analysis of ambient noise using seismic interferometry challenging.

Conversely, surface recordings show more energy variability in seismic background noise and higher power levels. The use of a large number of instruments at the surface allows also for a greater reduction in ambient noise by waveform stacking, if the waveforms are consistent across the array, individual arrivals can be aligned, and signal strengths exceed the instrument noise level. Therefore, a clear understanding of instrument self-noise levels is an important parameter in microseismic analyses for both borehole and surface deployments.

Knowledge of the instrument self-noise and the ambient noise level can also aid in event detection, since it permits to extract signals that are statistically different from the background PSD at individual frequencies. This has the advantage over STA/LTA method that no prior bandpass filtering is required to enhance the SNR and also permits for detection of signals with characteristically different frequency contents if the background noise spectrum is stationary.

REFERENCES

Ackerley, N. & Spriggs, N., 2012. Importance of Pre-Frack Site Surveys and Broadband Seismometers to Microseismic Monitoring, *Presented at CSEG Conference, GeoConvention 2012,* Calgary, Canada.

Allen, R.V., 1978. Automatic earthquake recognition and timing from single traces, *Bull. seism. Soc. Am.,* **68,** 1521–1532.

Bakulin, A. & Calvert, R., 2004. Virtual source: new method for imaging and 4D below complex overburden, in *Proceedings of the 74th Annual International Meeting,* SEG, Expanded Abstracts, Vol. 23, pp. 2477–2480.

Bensen, G.D., Ritzwoller, M.H., Barmin, M.P., Levshin, A.L., Lin, F., Moschetti, M.P., Shapiro, N.M. & Yang, Y., 2007. Processing seismic ambient noise data to obtain reliable broad-band surface wave dispersion measurements, *Geophys. J. Int.,* **169,** 1239–1260.

Berger, J., Davis, P. & Ekström, G., 2004. Ambient Earth noise: A survey of the Global Seismographic Network, *J. geophys. Res.,* **109,** B11307, doi:10.1029/2004JB003408.

Bonnefoy-Claudet, S., Cotton, F. & Bard, P.-Y., 2006. The nature of noise wavefield and its applications for site effects studies: a literature review, *Earth-Sci. Rev.,* **79,** 205–227.

Carter, J.A., Barstow, N., Pomeroy, P.W., Chael, E.P. & Leahy, P.J., 1991. High-frequency seismic noise as a function of depth, *Bull. seism. Soc. Am.,* **81,** 1101–1114.

Eaton, D.W., Van der Baan, M., Tary, J-B., Birkelo, B., Spriggs, N., Cutten, S. & Pike, K., 2013. Broadband microseismic observations from a Montney hydraulic fracture treatment, northeastern B.C., Canada, CSEG Recorder, 44–53.

Edwards, D.E., Barclay, J.E., Gibson, D.W., Kvill, G.E. & Halton, E., 2012. Triassic Strata of the Western Canada Sedimentary Basin, in *Proceedings of the Geological Atlas of the Western Canada Sedimentary Basin,* pp. 259–276, Alberta Geological Survey.

Eisner, L., Maxwell, S., Raymer, D., Williams, M. & Primiero, P., 2013. Signals, *Leading Edge,* **32,** 868–868.

Ewing, W.M., Jardetzky, W.S. & Press, F., 1957. *Elastic Waves in Layered Media,* McGraw-Hill Book Company Inc.

Goertz, A., Cieslik, K., Hauser, E., Watts, G., McCrossin, S. & Zbasnik, P., 2011. A combined borehole/surface broadband passive seismic survey over a gas storage field, in *Proceedings of the 81st Annual International Meeting,* SEG, Expanded Abstracts, Vol. 30, pp. 1488–1492.

Goertz, A., Riahi, N., Kraft, T. & Lambert, M., 2012. Modeling detection thresholds of microseismic monitoring networks, in *Proceedings of the 82nd Annual International Meeting,* SEG, Expanded Abstracts, Vol. 31, pp. 1–6, doi:10.1190/segam2012-1069.1.

Grechka, V. & Zhao, Y., 2012. Microseismic interferometry, *Leading Edge,* **31,** 1478–1483.

Hutt, C.R., Nigbor, R.L. & Evans, J., 2009. Proceedings of the guidelines for seismometer testing workshop, Albuquerque, New Mexico, 9–10 May 2005 ("GST"), USGS Open-File Report, 2009–1055, 48p.

Larose, E., Derode, A., Campillo, M. & Fink, M., 2004. Imaging from one-bit correlations of wideband diffuse wave fields, *J. appl. Phys.,* **95,** 8393–8399.

Lee, A.W., 1935. On the direction and approach of microseismic waves, *Proc. R. Soc. Lond., A, Math. Phys. Sci.,* **149,** 183–199.

Maxwell, S.C., White, D.J. & Fabriol, H., 2004. Passive seismic imaging of CO2 sequestration at Weyburn, in *Proceedings of the 74th Annual International Meeting,* SEG, Expanded Abstracts, Vol. 23, pp. 568–571.

Maxwell, S.C., Underhill, B., Bennett, L., Woerpel, C. & Martinez, A., 2010a. Key criteria for a successful microseismic project, in *Proceedings of the SPE Annual Technical Conference and Exhibition,* Vol. 4, pp. 3193–3208.

Maxwell, S.C., Rutledge, J., Jones, R. & Fehler, M., 2010b. Petroleum reservoir characterization using downhole microseismic monitoring, *Geophysics,* **75,** 75A 129–75A 137.

Maxwell, S.C., Raymer, D., Williams, M. & Primiero, P., 2012. Tracking microseismic signals from the reservoir to surface, *Leading Edge,* **31,** 1300–1308.

McNamara, D.E. & Buland, R.P., 2004. Ambient noise levels in the continental United States, *Bull. seism. Soc. Am.,* **94,** 1517–1527.

Miyazawa, M., Snieder, R. & Venkataraman, A., 2008. Application of seismic interferometry to extract P- and S-wave propagation and observation of shear-wave splitting from noise data at Cold Lake, Alberta, Canada, *Geophysics,* **73,** D35–D40.

Nofal, H.A.-E.M., Ahmed, E.M., Al Geldawy, F.A.-E. & Hafiz, A.G.R., 2004. Near optimum detection of the p-wave arrival using the spectrograms, in *Proceedings, International Conference on Electrical, Electronic and Computer Engineering, ICEEC'04,* pp. 710–715.

Ozbek, A., Probert, T., Raymer, D. & Drew, J., 2013. Nonlinear processing methods for detection and location of microseismic events, in *Proceedings of 75th EAGE Conference and Exhibition,* London, UK.

Peterson, J., 1993. Observations and modeling of seismic background noise, USGS Open-File Report, pp. 093–322.

Phillips, W.S., Rutledge, J.T. & House, L., 2002. Induced microearthquake patterns in hydrocarbon and geothermal reservoirs: six case studies, *Pure appl. Geophys.,* **159,** 345–369.

Riedesel, M.A., Moore, R.D. & Orcutt, J.A., 1990. Limits of sensitivity of inertial seismometers with velocity transducers and electronic amplifiers, *Bull. seism. Soc. Am.,* **80,** 1725–1752.

Ringler, A. & Hutt, C., 2010. Self-noise models of seismic instruments, *Seism. Res. Lett.,* **81,** 972–983.

Shemeta, J.E. *et al.*, 2009. Stacking seismograms to improve microseismic images, *SPE Prod. Operat.,* **24,** 156–164.

Stephen, R.A. *et al.*, 1994. The seafloor borehole array seismic system (SEABASS) and VLF ambient noise, *Mar. Geophys. Res.,* **16,** 243–286.

Trnkoczy, A., 2002. Understanding and parameter setting of STA/LTA trigger algorithm, in *IASPEI New Manual of Seismological Observatory Practice2,* pp. 1–20, ed. Bormann, P., doi:10.2312/GFZ.NMSOP-2_IS_8.1.

van der Baan, M., Eaton, D.W. & Dusseault, M., 2013. Microseismic Monitoring Developments in Hydraulic Fracture Stimulation, in *Effective and Sustainable Hydraulic Fracturing,* pp. 439–456, eds Bunger, A.P., McLennan, J. & Jeffrey, R., InTech.

Warpinski, N.R., 2009. Microseismic monitoring: inside and out, *J. Petrol. Technol.,* **61,** 80–85.

Warpinski, N.R., Mayerhofer, M.J., Vincent, M.C., Cipolla, C.L. & Lolon, E.P., 2009. Stimulating unconventional reservoirs: maximizing network growth while optimizing fracture conductivity, *J. Can. Petrol. Technol.,* **48,** 39–51.

Welch, P.D., 1967. The use of fast Fourier transform for the estimation of power spectra: a method based on time averaging over short, modified periodograms, *IEEE Trans. Audio Electroacoust.,* **15,** 70–73.

Withers, M., Aster, R., Young, C., Beiriger, J., Harris, M., Moore, S. & Trujillo, J., 1998. A comparison of select trigger algorithms for automated global seismic phase and event detection, *Bull. seism. Soc. Am.,* **88,** 95–106.